

Time-Aware One Step Diffusion Network for Real-World Image Super-Resolution

Tainyi Zhang¹ Zheng-Peng Duan¹ Peng-Tao Jiang² Bo Li²
Ming-Ming Cheng² Chun-Le Guo^{1,3*} Chongyi Li^{1,3}

¹VCIP, CS, Nankai University ²vivo Mobile Communication Co. Ltd ³NKIARI, Shenzhen Futian
zty557@gmail.com, adamduan0211@gmail.com, pt.jiang@vivo.com, libra@vivo.com,
{cmm, guochunle, lichongyi}@nankai.edu.cn

Project page: https://zty557.github.io/TADSR_HomePage/

Abstract

Diffusion-based real-world image super-resolution (Real-ISR) methods have demonstrated impressive performance. To achieve efficient Real-ISR, many works employ Variational Score Distillation (VSD) to distill pre-trained stable-diffusion (SD) model for one-step SR with a fixed timestep. However, due to the different noise injection timesteps, the SD will perform different generative priors. Therefore, a fixed timestep is difficult for these methods to fully leverage the generative priors in SD, leading to suboptimal performance. To address this, we propose a **Time-Aware** one-step Diffusion Network for Real-ISR (**TADSR**). We first introduce a Time-Aware VAE Encoder, which projects the same image into different latent features based on timesteps. Through joint dynamic variation of timesteps and latent features, the student model can better align with the input pattern distribution of the pre-trained SD, thereby enabling more effective utilization of SD’s generative capabilities. To better activate the generative prior of SD at different timesteps, we propose a Time-Aware VSD loss that bridges the timesteps of the student model and those of the teacher model, thereby producing more consistent generative prior guidance conditioned on timesteps. Additionally, though utilizing the generative prior in SD at different timesteps, our method can naturally achieve **controllable trade-offs between fidelity and realism** by changing the timestep condition. Experimental results demonstrate that our method achieves both state-of-the-art performance and controllable SR results with only a single step.

Introduction

Image Super-Resolution (ISR) aims to reconstruct a high-quality (HQ) image from its low-quality (LQ) counterpart. Different from the simple degradation assumptions in traditional ISR (Lim et al. 2017; Zhang et al. 2018b; Chen et al. 2021; Liang et al. 2021; Chen et al. 2023; Dong et al. 2014), Real-World Image Super-Resolution (Real-ISR) aims to restore HQ images from LQ inputs degraded by complex and unknown factors in real-world scenarios, which has recently attracted increasing attention (Wang et al. 2021; Xie et al. 2023; Zhang et al. 2021; Liang, Zeng, and Zhang 2022).

*Corresponding author.

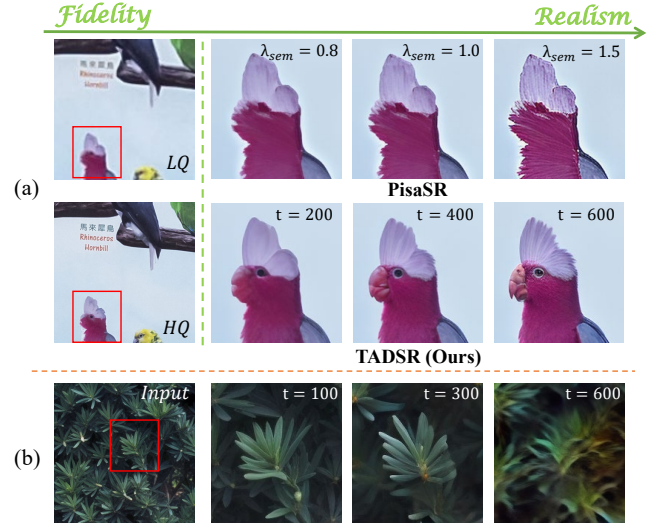


Figure 1: (a) Comparison between our TADSR and PisaSR. In PisaSR, increasing the semantic weight λ_{sem} leads to the restoration of more realistic images. As the timestep condition t_s increases, our model demonstrates a significant improvement in generative capability, recovering a more realistic parrot image. In contrast, PisaSR shows only an increase in sharpness as λ_{sem} increases. (b) The input image and the corresponding outputs of the teacher model at different timesteps t with the VSD loss. The outputs of the teacher model vary significantly across different timesteps, reflecting distinct guidance orientations.

To address a broader spectrum of degradation types and achieve more realistic results, many researchers have turned to generative models. Recently, diffusion models (Ho, Jain, and Abbeel 2020) have demonstrated a superior ability to generate fine-grained details in image generation tasks. Consequently, several works have explored leveraging the generative priors in pre-trained Stable Diffusion (SD) models (Rombach et al. 2022) to tackle Real-ISR, yielding impressive results (Wang et al. 2023a; Lin et al. 2023; Tao et al. 2023; Wu et al. 2024c; Duan et al. 2025). Nevertheless, the iterative denoising process inherent in diffusion models introduces significant computational overhead and latency.

To overcome these limitations, some researchers have focused on distilling SD into an efficient one-step model for Real-ISR (Wu et al. 2024b; Sun et al. 2025; Chen et al. 2025; Dong et al. 2025; Zhang et al. 2024). Specifically, OSEDiff (Wu et al. 2024b) first leverages the Variational Score Distillation (VSD) loss (Wang et al. 2023b) to distill the SD model, enabling realistic image reconstruction in a single step. Subsequently, S3Diff (Zhang et al. 2024), PisaSR (Sun et al. 2025), AdcSR (Chen et al. 2025), and TSDSR (Dong et al. 2025) also adopt distillation-based approaches to develop SD-based one-step Real-ISR models, using either adversarial loss or modified VSD loss.

However, these works generally fix the injected timestep, e.g. step 999, and use the original VAE encoder in SD, which prevent them from effectively leveraging the generative prior in SD. Specifically, as shown in Fig. 1(b), the output of the teacher model (pre-trained SD) varies depending on the input timestep and latent features. When timestep t equals 100, there are only differences in texture details between the output of the teacher model and the input image. In contrast, when t increases to 300, the output shows clear differences, reflecting more of the leaf-related semantic prior learned by SD. However, with t increasing further to 600, most of the image information is lost, and the teacher model can only recover the overall structure and color of the leaves, failing to provide meaningful guidance. These observations imply that fixed timestep and latent features are insufficient to fully activate the generative priors across different timesteps in SD, the gradient guidance from the teacher model is also timestep-dependent. As a result, as shown in Fig. 1(a), although we increase the semantic weight λ_{sem} in PisaSR (Sun et al. 2025), it only produces enhanced sharpness without significantly enriching the semantic content.

In this paper, we propose Time-Aware One Step Diffusion Network for Super-Resolution (TADSR), a framework that more effectively distills the generative prior of SD at different timesteps into a one-step diffusion model for Real-ISR. Our TADSR consists of two key components: (1) Time-Aware VAE Encoder (TAE): we introduce a time embedding layer into the VAE encoder, enabling it to map the same image to different latent representations based on the timestep, thereby achieving coordinated adjustment between the timestep and latent representation. Through the TAE, we can establish a matching relationship between the input timestep and latent representation similar to that in the original SD, allowing for more effective utilization of the generative priors of SD at different timesteps. (2) Time-Aware Variational Score Distillation (TAVSD) Loss: we design a mapping function to associate the timestep injected into the SR network with the one used in the VSD loss. When the SR network is conditioned on a larger timestep, the teacher receives a latent image corrupted with stronger noise, providing guidance that emphasizes stronger semantic generation in the reconstruction results. Conversely, smaller timesteps lead to similar results with reconstruction, primarily enhancing texture details. Therefore, TAVSD can provide more consistent generative guidance condition on the injected timestep in the SR network.

Thanks to TAE and TAVSD, the proposed TADSR can

naturally leverage the generative priors of SD at different timesteps to achieve controllable trade-offs between fidelity and realism in Real-ISR and superior performance. As shown in Fig. 1(a), our method gradually generates a more realistic parrot as the timestep increases, though fully leveraging the generative priors in SD.

Related Work

Real-World Image Super-Resolution

Traditional ISR methods (Lim et al. 2017; Zhang et al. 2018b; Chen et al. 2021; Liang et al. 2021; Chen et al. 2023; Dong et al. 2014; Zhao et al. 2025) typically degrade HQ images using simple downsampling operations to construct HQ-LQ image pairs for training, supervised by pixel-level losses. However, these approaches struggle to handle images degraded by complex real-world processes and often result in overly smooth reconstructions. To better simulate the unknown and complex degradations in real-world scenarios, several studies (Zhang et al. 2021; Wang et al. 2021) have proposed more sophisticated degradation pipelines to synthesize LQ data. Specifically, BSRGAN (Zhang et al. 2021) introduces a random combination of basic degradation operations (e.g., downsampling, blurring, noise) injection, with varying intensities to generate more realistic HQ-LQ pairs. Real-ESRGAN (Wang et al. 2021) proposes a second-order degradation scheme to cover a broader range of degradation types. In addition, inspired by Generative Adversarial Networks (GANs), researchers have incorporated discriminators into Real-ISR frameworks and adopted adversarial losses to encourage the reconstruction of more realistic images. Although these GAN-based methods can produce richer texture details compared to traditional approaches, they are often unstable to train and prone to generating unnatural artifacts (Wu et al. 2024b).

Diffusion-Based Real-ISR

Recently, many researchers have leveraged the powerful generative priors of pre-trained diffusion models for Real-ISR tasks to achieve high-fidelity image reconstruction. For example, StableSR (Wang et al. 2023a) conditions the diffusion process on LQ images by injecting them through a learnable time-aware encoder into the SD model, enabling strong detail generation capabilities. DiffBIR (Lin et al. 2023) utilizes ControlNet to extract structural information from LQ images and incorporates it as a control signal to better guide the generative prior of SD for super-resolution. PASD (Tao et al. 2023) and SeeSR (Wu et al. 2024c) extract semantic information from LQ inputs and inject it into SD, resulting in more realistic super-resolved outputs.

Although these approaches yield impressive results, the multi-step denoising process leads to high computational and time costs. To accelerate diffusion-based Real-ISR, OSEDiff introduces the VSD loss to distill the pre-trained SD model, enabling realistic image reconstruction in a single step by only training LoRA parameters mounted on SD. S3Diff further adopts degradation-guided LoRA adapters combined with adversarial training to achieve one-step super-resolution. PisaSR trains two separate LoRA adapters

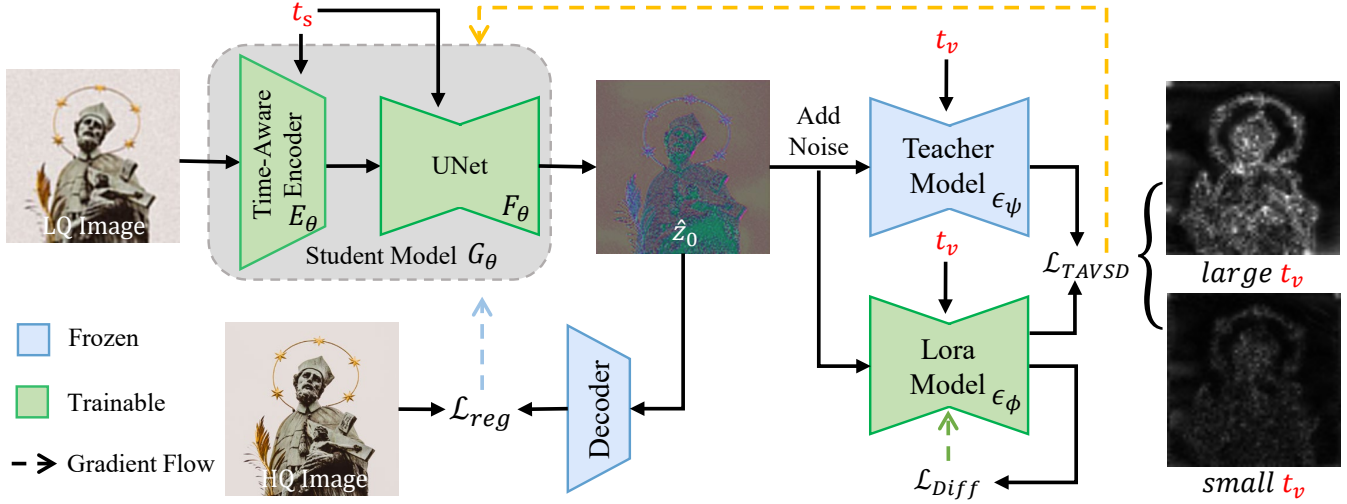


Figure 2: Overview of TADSR. We train a Student Model G_θ to perform one-step Real-ISR, which consists of a Time-Aware VAE Encoder E_θ and a UNet F_θ . We randomly sample a timestep t_s and map it to t_v . The t_s and the LQ image are fed into the encoder E_θ to obtain the LQ latent. Then, t_s and the LQ latent are fed into the UNet F_θ to produce the reconstructed latent feature \hat{z}_0 . After adding noise to \hat{z}_0 corresponding to t_v , we feed it and t_v into the teacher model and the LoRA model to compute the TAVSD loss (orange flow). The reconstruction loss (blue flow) in pixel space and TAVSD loss is then used to jointly update the student model G_θ . For the LoRA Model, we employ the diffusion loss (green flow) for training.

for pixel-level and semantic-level guidance, allowing controllable trade-offs between realism and fidelity.

However, these methods overlook the varying generative capabilities of SD in different timesteps: larger timesteps favor semantic and structural generation, while smaller timesteps emphasize texture and detail. Our work aims to fully exploit these time-dependent generation characteristics to achieve superior SR performance and a natural balance between visual fidelity and generative realism.

Methodology

Problem Definition

Real-ISR aims to reconstruct HQ images x_H from LQ images x_L that suffer from complex and unknown degradations. With the advancement of deep learning, researchers have commonly adopted neural networks G_θ to estimate the HQ images and optimize the network through loss functions. The general form of the loss function is as:

$$\theta^* = \arg \min_{\theta} \mathbb{E}_{(x_L, x_H) \sim \mathcal{D}} [\mathcal{L}_{Rec}(G_\theta(x_L), x_H) + \lambda \mathcal{L}_{Reg}(G_\theta(x_L))], \quad (1)$$

where the \mathcal{L}_{Rec} denotes the reconstruction loss to optimize the fidelity of the reconstructed results. \mathcal{L}_{Reg} is the regression loss to enhance the realism of the results, and λ is a hyperparameter to balance \mathcal{L}_{Rec} and \mathcal{L}_{Reg} .

Recently, with the advancement of diffusion models, several studies (Wu et al. 2024b; Sun et al. 2025) have leveraged the generative prior in pre-trained SD and adopted VSD as a regression objective. The formation of VSD is:

$$\nabla_{\theta} \mathcal{L}_{VSD}(\hat{z}, c) = \mathbb{E}_{t, \epsilon} \left[\omega(t) (\epsilon_\psi(\hat{z}_t; t, c) - \epsilon_\phi(\hat{z}_t; t, c)) \frac{\partial \hat{z}}{\partial \theta} \right], \quad (2)$$

where ϵ_ψ is the pre-trained diffusion model (teacher model), ϵ_ϕ represents its replica with trainable LoRA (LoRA model), and c is a text embedding of a caption describing the input image. $\hat{z} = G_\theta(x_L)$ is the output of the student network G_θ , and $\hat{z}_t = \alpha_t \hat{z} + \beta_t \epsilon$ is the noisy latent input. ϵ is the gaussian noise, and α_t and β_t are the scale parameters in diffusion.

Formally, the VSD loss can be viewed as the residual between the noise outputs of the teacher model and the LoRA model, which is equivalent to the residual of their predicted latent images (detailed proof can be found in **supplementary material**). Therefore, in the following, we represent the VSD loss using the latent images and their residual.

Overview

As illustrated in Fig. 2, we distill a Student Model G_θ to perform one-step Real-ISR, which is consist of a Time-Aware Encoder E_θ and a UNet F_θ . First, we sample an HQ-LQ image pair from the dataset and a timestep t_s . Then, both the LQ image and t_s are fed into Student Model G_θ to obtain the latent output \hat{z}_0 . We decode \hat{z}_0 into pixel space and compute the reconstruction loss with the HQ image to ensure fidelity. In the latent space, we map the t_s to another timestep t_v , and add noise corresponding to timestep t_v to the \hat{z}_0 to obtain \hat{z}_{t_v} . Then, we feed \hat{z}_{t_v} and t_v into both the teacher model and the LoRA model to compute the Time-Aware Variational Score Distillation loss \mathcal{L}_{TAVSD} to enhance the realism. Consistent with Fig. 1(b), when t_v is small, the gradients produced by the TAVSD loss are relatively small and

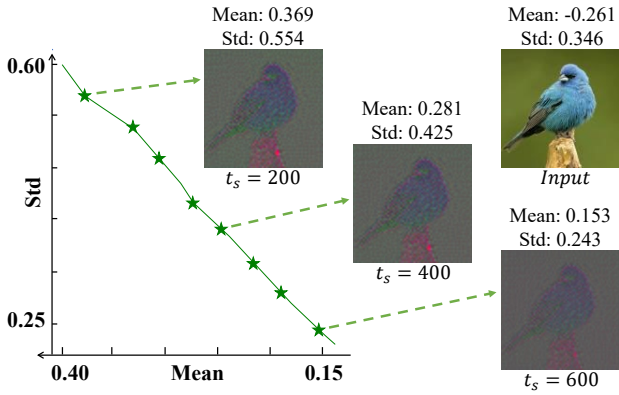


Figure 3: PCA visualization of latent features produced by TAE under different timesteps t_s , and the corresponding mean and standard deviation (Std) of latent features. TAE can encode the same image into distinct latent features conditioned on different timesteps, which aligns with the synchronized variation between timesteps and latent features in the pre-trained SD.

mainly reflect texture details. In contrast, when t_v is large, the gradients become significantly large and provide more semantic guidance.

Time-Aware VAE Encoder

In the original SD, as timestep increases, the latent features fed into the model are injected with more noise, thereby activating different generative priors to produce the image. However, current one-step SD-based Real-ISR methods typically adopt a fixed timestep during training, making it difficult to fully exploit the generative priors in SD. Since the original VAE encoder can only encode the same image into a single latent feature, simply sampling the timestep randomly is insufficient, which is clearly inconsistent with the correlation between timesteps and latent distributions in SD.

To better utilize the generative priors in SD, we propose a Time-Aware VAE Encoder (TAE). By incorporating a temporal embedding layer into the VAE encoder, TAE encodes the input image into different latent distributions conditioned on the timestep t_s , enabling synchronized variation between t_s and latent distribution, thus better activating the generative priors at different timesteps within SD. This process can be formulated as:

$$z_L = E_\theta(x_L, t_s), \hat{z} = F_\theta(z_L, t_s), \quad (3)$$

where E_θ is the TAE model and F_θ is the Unet model.

As shown in Fig. 3, with the same input image, TAE encodes it into different latent feature condition on the timestep t_s . Overall, as the t_s increases, both the mean and variance of the latent features show a decreasing trend. After visualizing the latent feature via PCA dimensionality reduction, we can also clearly observe the changes in the latent space.

Time-Aware Variational Score Distillation

Following the OSEDiff (Wu et al. 2024b), the VSD loss has been widely adopted in SD-based one-step Real-ISR meth-

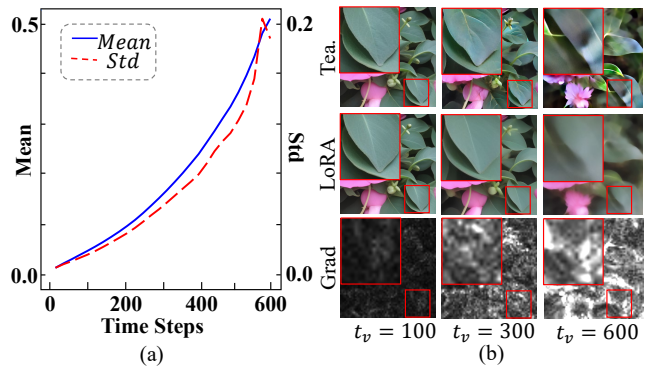


Figure 4: (a) Mean and standard deviation (Std) of the VSD loss at different timesteps. (b) The outputs of the teacher model and the LoRA model are decoded into pixel space and gradients in latent space at different timesteps t_v .

ods to enhance the realism of reconstruction results. However, these methods generally overlook that the guidance provided by VSD at different timesteps is actually inconsistent. As shown in Fig. 4, the mean and standard deviation of the VSD loss exhibit a clear upward trend as the timestep increases. When decoding the results at different timesteps into the pixel space, we observe that at t_v equals 100, the outputs of the teacher and LoRA models are similar, and the gradients mainly reflect enhancements in texture details. In contrast, when t_v increases to 300, the teacher model’s output contains significantly more semantic information while the LoRA model’s output remains smooth, and the gradients reflect global semantic guidance. However, when t_v increases to 600, the teacher model can only recover coarse color and structural information from the noisy latent input, making it difficult to provide meaningful guidance. This implies that the VSD loss provides distinct guidance for the same image depending on t_v . Such opposing directional guidance creates conflicting optimization signals for the student model, ultimately leading to suboptimal convergence.

This phenomenon arises because most of the image information is preserved when t is small, and both the teacher and LoRA models focus mainly on generating texture details. As t increases, the injection of more noise gradually obscures the underlying image content, forcing the teacher model to rely more heavily on its generative prior. However, since the LoRA model is trained on low-quality data generated by the student model and does not employ the CFG strategy (Ho and Salimans 2022), its outputs tend to be overly smooth.

Considering that the guidance provided by VSD varies across different timesteps, we establish a connection between the timestep t_s input to the student model and the timestep t_v in the teacher model, so that the VSD loss can provide more consistent gradient guidance conditioned on t_s . Specifically, we feed the randomly sampled t_s and the LQ image into the student model to obtain $\hat{z} = G_\theta(x_L, t_s)$. Then, t_s is mapped to t_v by:

$$t_v = \lambda t_s + \gamma, t_s \in [0, 999], \quad (4)$$

where the λ and γ are the hyperparameters.

Table 1: A comprehensive evaluation against state-of-the-art methods across synthetic and real-world datasets. The top-performing and runner-up results under each metric are marked in **red** and **blue**, respectively.

Datasets	Metrics	StableSR	DiffBIR	SeeSR	SinSR	S3Diff	OSDiff	PisaSR	TSDSR	AdcSR	TADSR
<i>DIV2k-Val</i>	PSNR \uparrow	23.261	23.409	23.679	24.417	23.530	23.723	<u>23.867</u>	22.17	23.743	23.815
	SSIM \uparrow	0.5726	0.5732	0.6043	0.6023	0.5933	0.6109	<u>0.6058</u>	0.5602	0.6017	0.6028
	LPIPS \downarrow	0.3113	0.3456	0.3194	0.3235	0.2581	0.2942	0.2823	<u>0.2736</u>	0.2853	0.3078
	CLIQQA \uparrow	0.6771	0.7082	0.6935	0.6505	0.7001	0.6682	0.6928	<u>0.7149</u>	0.6763	0.7353
	MUSIQ \uparrow	65.918	68.396	68.665	62.838	67.923	67.971	<u>69.681</u>	70.65	67.995	69.649
	MANIQA \uparrow	0.6174	0.6355	0.6222	0.5392	0.6311	0.6132	<u>0.6375</u>	0.6077	0.6073	0.6443
	TOPIQ \uparrow	0.5979	0.6344	<u>0.6856</u>	0.5721	0.6334	0.6188	0.6619	0.6672	0.6526	0.7044
	QALIGN \uparrow	3.5273	3.8774	<u>3.9765</u>	3.5159	3.8666	3.8357	3.8812	3.927	3.612	4.0783
<i>DRealSR</i>	PSNR \uparrow	28.030	25.929	28.073	<u>28.345</u>	27.539	27.915	28.318	26.20	28.099	28.387
	SSIM \uparrow	0.7536	0.6526	0.7684	0.7491	0.7491	0.7833	<u>0.7804</u>	0.7170	0.7726	0.7758
	LPIPS \downarrow	0.3284	0.4518	0.3173	0.3697	0.3109	<u>0.2968</u>	0.2960	0.3116	0.3046	0.3235
	CLIQQA \uparrow	0.6356	0.6863	0.6909	0.6375	0.7131	0.6974	0.6971	<u>0.7309</u>	0.7049	0.7398
	MUSIQ \uparrow	58.512	65.667	65.080	55.009	63.941	64.691	66.113	66.12	<u>66.266</u>	67.016
	MANIQA \uparrow	0.5594	<u>0.6289</u>	0.6051	0.4894	0.6124	0.5903	0.6160	0.5820	0.5915	0.6309
	TOPIQ \uparrow	0.5323	0.6149	<u>0.6575</u>	0.5122	0.6040	0.6002	0.6333	0.6251	0.6527	0.6758
	QALIGN \uparrow	3.0614	3.6011	3.5882	3.0982	3.6148	3.5450	3.5838	3.6928	<u>3.6520</u>	3.7491
<i>RealSR</i>	PSNR \uparrow	24.645	24.240	25.149	26.266	25.183	25.148	<u>25.503</u>	23.404	25.469	25.166
	SSIM \uparrow	0.7080	0.6649	0.7211	<u>0.7341</u>	0.7269	0.7338	0.7418	6886	0.7301	0.7150
	LPIPS \downarrow	0.3002	0.3470	0.3007	0.3241	<u>0.2721</u>	0.2920	0.2672	0.2805	0.2885	0.3168
	CLIQQA \uparrow	0.6234	0.6959	0.6699	0.6153	<u>0.6731</u>	0.6687	0.6699	<u>0.7199</u>	0.6731	0.7283
	MUSIQ \uparrow	65.883	68.340	69.819	60.575	65.824	69.087	70.147	<u>70.7710</u>	69.899	71.182
	MANIQA \uparrow	0.6230	0.6530	0.6450	0.5409	0.6427	0.6337	<u>0.6551</u>	0.6311	0.6353	0.6715
	TOPIQ \uparrow	0.5748	0.6052	<u>0.6890</u>	0.5188	0.6162	0.6251	0.6374	0.6642	0.6793	0.7082
	QALIGN \uparrow	3.2767	3.6313	3.7190	3.1889	3.6638	3.6915	3.6355	3.7748	<u>3.7749</u>	3.9477
<i>RealLR200</i>	CLIQQA \uparrow	0.6036	0.7072	0.7023	0.6474	0.7122	0.6792	0.7153	<u>0.7248</u>	0.7048	0.7741
	MUSIQ \uparrow	62.863	67.727	70.195	63.126	68.897	69.041	<u>70.935</u>	70.930	69.759	72.166
	MANIQA \uparrow	0.5922	0.6464	0.6482	0.5522	0.6536	0.6331	<u>0.6639</u>	0.6363	0.6354	0.6738
	TOPIQ \uparrow	0.5286	0.5905	<u>0.6900</u>	0.5689	0.6401	0.5990	0.6627	0.6664	0.6684	0.7249
	QALIGN \uparrow	3.3409	3.7782	<u>4.0305</u>	3.4105	3.9228	3.8459	3.9891	3.8908	3.9312	4.2622

We then add noise to \hat{z} corresponding to t_v to obtain $\hat{z}_{t_v} = \alpha_{t_v} \hat{z} + \beta_{t_v} \epsilon$, which is then passed through the teacher model and the LoRA model with t_v to compute the TAVSD loss:

$$\nabla_{\theta} \mathcal{L}_{TAVSD}(\hat{z}, c, t_v) = \mathbb{E}_{\epsilon} [\omega(t_v) (\epsilon_{\psi}(\hat{z}_{t_v}; t_v, c) - \epsilon_{\phi}(\hat{z}_{t_v}; t_v, c)) \frac{\partial \hat{z}}{\partial \theta}]. \quad (5)$$

By leveraging the TAVSD loss, the model can naturally balance generation and fidelity in the Real-ISR task simply by varying the timestep condition t_s input to the model.

Training Loss

We train the student model with reconstruction and regression losses. To avoid gradient inconsistency arising from the ill-posed problem of the Real-ISR task (Liang, Zeng, and Zhang 2022) while fully leveraging the teacher model knowledge introduced by VASVD, we first apply a Gaussian blur to both the reconstructed image and the HQ image x_H

before computing the MSE loss. This ensures that the x_H only supervises the low-frequency content of the reconstruction, helping to preserve high-frequency details. We adopt a larger blur kernel for larger timesteps t_s , which enhances the trade-off between fidelity and generation:

$$\mathcal{L}_{MSE}^{blur} = \mathcal{L}_{MSE}(G_{\theta}(x_L) * G_{t_s}, x_H * G_{t_s}). \quad (6)$$

Where $*$ denotes the convolution operation, G_{t_s} is the convolution kernel whose size is determined by t_s . This loss and the LPIPS loss, forms the reconstruction loss:

$$\mathcal{L}_{Rec} = \mathcal{L}_{MSE}^{blur} + \mathcal{L}_{LPIPS}(G_{\theta}(x_L), x_H). \quad (7)$$

For the regression loss, we adopt the TAVSD loss in Eq. 5 to improve the realism of the generated results. The overall loss for the student model is:

$$\mathcal{L}_{Stu} = \mathcal{L}_{Rec} + \lambda_{TAVSD} \cdot \mathcal{L}_{TAVSD}. \quad (8)$$

For the LoRA model, we adopt the original diffusion loss:

$$\mathcal{L}_{Diff}(\hat{z}, c_y) = \mathbb{E}_{t, \epsilon} [\|\epsilon_{\phi}(\hat{z}_t; t, c_y) - \epsilon'\|^2], \quad (9)$$

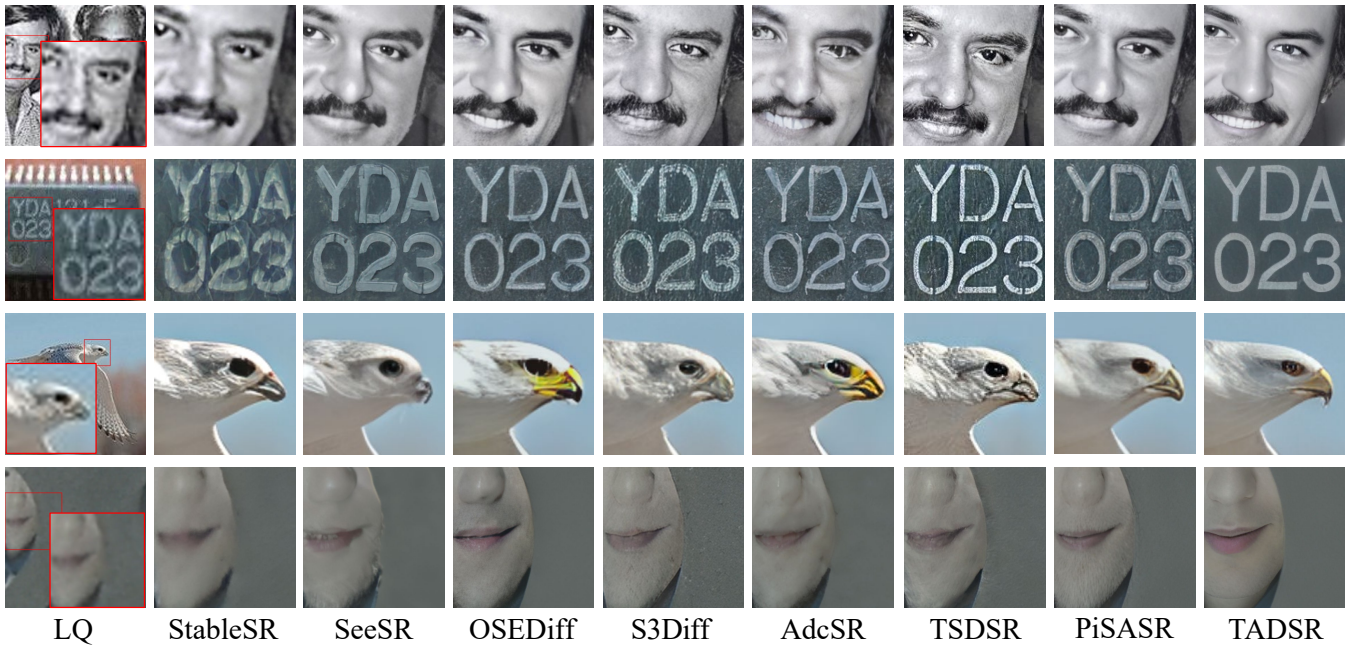


Figure 5: Visual comparisons between our method and other Real-ISR methods. Please zoom in for a better view.

where ϵ' is the Gaussian noise as the training target for the denoising network.

Experiments

Experimental Setup

Training. We use LSDIR (Li et al. 2023) as the training data with the 512×512 patch size. To generate paired HQ-LQ training data, we follow the degradation pipeline from Real-ESRGAN (Wang et al. 2021). We use AdamW optimizer (Loshchilov and Hutter 2017) with a learning rate 5×10^{-5} and set LoRA rank to 4 for both the student model and LoRA model. We employ the SD 2.1-base as the pre-trained diffusion model and fine-tune it for 2k iterations using 8 NVIDIA A40 GPUs with a batch size of 24.

Test Dataset. We evaluate our method in both synthetic and real-world dataset. For the synthetic dataset, we randomly crop 3K patches with a resolution of 512×512 from the DIV2K (Agustsson and Timofte 2017) validation set and synthesize LQ data using the same pipeline as that in training. For real-world data, we employ RealSR (Cai et al. 2019), DrealSR (Wei et al. 2020), and ReallR200 (Wu et al. 2024c). We center-crop RealSR (Cai et al. 2019) and DrealSR (Wei et al. 2020) datasets with size 128×128 for LQ images and 512×512 for HQ image. For ReallR200 (Wu et al. 2024c) dataset, since the corresponding HQ images are unavailable, we perform only a 128×128 center-crop on the LQ images.

Evaluation Metrics. We utilize several reference and non-reference metrics to evaluate the performance of various methods on the test data. For the reference measures, we employ PSNR, SSIM (Wang et al. 2004), and LPIPS (Zhang et al. 2018a) to measure image fidelity. For the non-reference

measures, we employ CLIPQA (Wang, Chan, and Loy 2023), MUSIQ ((Ke et al. 2021), MANIQA (Yang et al. 2022), TOPIQ (Chen et al. 2024), and QALIGN (Wu et al. 2024a) to measure image quality.

Compared Methods. We compare our method with several multi-step diffusion-based methods StableSR (Wang et al. 2023a), DiffBIR (Lin et al. 2023), SeeSR (Wu et al. 2024c), and one-step diffusion-based methods SinSR (Wang et al. 2024), OSEDiff (Wu et al. 2024b), S3Diff (Zhang et al. 2024), AdcSR (Chen et al. 2025), TSDSR (Dong et al. 2025), and PisaSR (Sun et al. 2025). All comparative results are obtained using publicly released code for testing.

Comparisons with State-of-the-art Methods

Quantitative Comparisons. We set up the timestep condition $t_s = 500$ in our method, and show the quantitative comparisons on the four synthetic and real-world datasets in Tab. 1. We have the following observations: (1) TADSR achieves the highest no-reference scores across four datasets, except for the MUSIQ on DIV2K-Val. This demonstrates that TADSR can more effectively leverage the generative priors from SD to produce more realistic results. Notably, TADSR is the only one-step methods that consistently outperforms multi-step methods on all no-reference metrics, achieving both efficiency and perceptual quality. (2) TADSR maintains PSNR values comparable to other SD-based one-step methods, indicating a good balance between fidelity and realism. (3) TADSR shows clear improvements over other SD-based one-step methods on CLIPQA and TOPIQ, highlighting its superior semantic awareness and generative capability.

Qualitative Comparisons. Fig. 5 shows the visual comparisons between our method and the other state-of-the-art

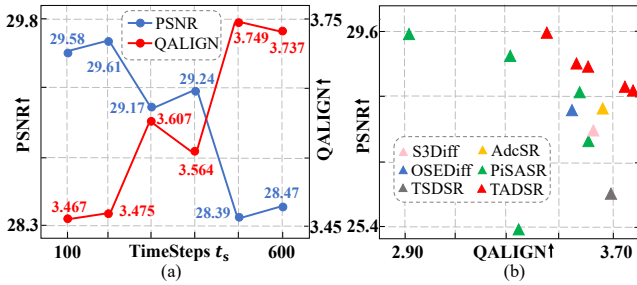


Figure 6: (a) Quantitative metrics of our method under different timestep condition t_s , evaluated on the *DrealSR* dataset. (b) Comparison of our method under different timesteps t_s , PisaSR under different semantic guidance weights λ_{sem} , and other one-step diffusion-based Real-ISR methods, evaluated on the *DrealSR* dataset.

Real-ISR methods. As shown in the first row, TADSR generates significantly more natural and sharper textures from heavily degraded LQ images, especially in facial regions such as the teeth, eyes, and eyebrows, demonstrating its strong semantic generation capability. In the second row, the digits and letters produced by TADSR appear much clearer, showcasing its superior degradation removal ability while preserving fidelity. In the third row, TADSR yields more natural results around the eagle’s eyes and beak. In the fourth row, only TADSR accurately restored natural-looking facial features such as the nose, mouth, and chin. Other methods generally suffered from degradation, resulting in some distortion, and failed to reconstruct a plausible chin structure. Overall, thanks to the ability to distill generative priors from SD more effectively in TAVSD loss, TADSR can produce natural and realistic results in a single diffusion step. Compared to other methods, it achieves strong perceptual quality while maintaining high efficiency.

Ablation Study

Impact of Different Timestep Condition. As shown in Fig. 6(a), we analyze the impact of timestep t_s in our method on both reference and no-reference metrics. As t_s increases, PSNR exhibits a decreasing trend while QALIGN shows an upward trend, indicating a trade-off where fidelity is sacrificed to enhance realism. This trade-off between fidelity and realism aligns with the function of t_s , as a larger t_s means that TAVSD provides stronger generative guidance, while a smaller t_s provides more fidelity-preserving guidance. Similar visual results can be observed in **supplementary materials**. Furthermore, we compare the results of our method under different t_s , PisaSR under different λ_{sem} settings, and other one-step Real-ISR methods, as shown in Fig. 6(b). It can be observed that our method consistently lies in the top-right corner across different t_s . When t_s equals 200, our method achieves 26.61dB PSNR, which is more than 1dB higher than SinSR, and QALIGN is significantly higher than SinSR. In contrast, although PisaSR can also achieve a PSNR of 29.60dB by tuning the $\lambda_{pix} = 1.0$ and $\lambda_{sem} = 0.6$, its QALIGN is only 2.91, which is similar to SinSR. This in-



Figure 7: Vision Comparisons of the ablation study on TAE and TAVSD. Baseline use the original VAE encoder in SD and VSD loss.

Dataset	Method	PSNR \uparrow	MUSIQ \uparrow	CLIPQA \uparrow	TOPIQ \uparrow
RealSR	Baseline	24.39	70.22	0.6751	0.6391
	w/o TAE	24.89	70.08	0.6857	0.6466
	w/o TAVSD	24.84	70.96	0.6930	0.6553
	Full	25.16	71.18	0.7283	0.7082
DrealSR	Baseline	27.45	65.90	0.6887	0.6275
	w/o TAE	27.95	65.95	0.7030	0.6396
	w/o TAVSD	28.03	66.95	0.7015	0.6373
	Full	28.39	67.02	0.7398	0.6758

Table 2: Quantitative Comparison of ablation study on TAVSD and TAE. Baseline uses the original VAE encoder in SD and VSD loss.

icates that our method achieves a substantial improvement in fidelity with only a minimal compromise in realism.

Impact of TAVSD and TAE. To validate the effectiveness of TAVSD and TAE, we conducted ablation studies by removing them. We employ the original VAE encoder in SD and the VSD loss as our baseline and conduct ablation studies by separately removing TAE and TAVSD. We use PSNR to evaluate fidelity and MANIQA, MUSIQ, and TOPIQ to assess realism. As shown in Tab. 2, we have the following three key observations: (1) After removing TAE, both reference and no-reference metrics decline, demonstrating that adapting the latent feature according to timesteps helps more fully utilize the generative priors in SD. (2) When TAVSD is ablated, all metrics similarly decrease, indicating that more consistent guidance from the teacher model better activates generative priors across different timesteps. (3) Baseline shows significant degradation in PSNR and moderate decline in others, proving that both TAE and TAVSD improve fidelity and realism. Additionally, Fig. 7 presents a visual comparison of our ablation studies, showing that both the absence of TAE/TAVSD leads to unrealistic parrot reconstructions while the baseline even produces visible artifacts. In contrast, our method produces realistic and natural results by fully exploiting the generative priors in SD.

Conclusion

In this paper, we propose TADSR, a one-step SD-based Real-ISR method. TADSR introduces a variable timestep t_s into the student model and uses a Time-Aware VAE Encoder to fully utilize the generative priors in SD at different timesteps. To further distill the priors at different timesteps in SD to achieve varied SR effects, TADSR leverages the Time-Aware Variational Score Distillation to enable the teacher model to provide more consistent generative guidance condition on t_s . As a result, TADSR fully lever-

ages the generative priors in SD and naturally achieves a controllable trade-off between fidelity and realism condition on t_s . Our experiments demonstrate that TADSR achieves state-of-the-art performance among all Real-ISR methods.

References

- Agustsson, E.; and Timofte, R. 2017. Ntire 2017 challenge on single image super-resolution: Dataset and study. In *CVPRW*, 126–135.
- Cai, J.; Zeng, H.; Yong, H.; Cao, Z.; and Zhang, L. 2019. Toward real-world single image super-resolution: A new benchmark and a new model. In *ICCV*, 3086–3095.
- Chen, B.; Li, G.; Wu, R.; Zhang, X.; Chen, J.; Zhang, J.; and Zhang, L. 2025. Adversarial diffusion compression for real-world image super-resolution. In *Proceedings of the Computer Vision and Pattern Recognition Conference*, 28208–28220.
- Chen, C.; Mo, J.; Hou, J.; Wu, H.; Liao, L.; Sun, W.; Yan, Q.; and Lin, W. 2024. TOPIQ: A Top-Down Approach From Semantics to Distortions for Image Quality Assessment. *IEEE TIP*, 33: 2404–2418.
- Chen, H.; Wang, Y.; Guo, T.; Xu, C.; Deng, Y.; Liu, Z.; Ma, S.; Xu, C.; Xu, C.; and Gao, W. 2021. Pre-trained image processing transformer. In *CVPR*, 12299–12310.
- Chen, X.; Wang, X.; Zhou, J.; Qiao, Y.; and Dong, C. 2023. Activating more pixels in image super-resolution transformer. In *CVPR*, 22367–22377.
- Dong, C.; Loy, C. C.; He, K.; and Tang, X. 2014. Learning a deep convolutional network for image super-resolution. In *ECCV*, 184–199. Springer.
- Dong, L.; Fan, Q.; Guo, Y.; Wang, Z.; Zhang, Q.; Chen, J.; Luo, Y.; and Zou, C. 2025. Tsd-sr: One-step diffusion with target score distillation for real-world image super-resolution. In *Proceedings of the Computer Vision and Pattern Recognition Conference*, 23174–23184.
- Duan, Z.-P.; Zhang, J.; Jin, X.; Zhang, Z.; Xiong, Z.; Zou, D.; Ren, J.; Guo, C.-L.; and Li, C. 2025. DiT4SR: Taming Diffusion Transformer for Real-World Image Super-Resolution. *arXiv preprint arXiv:2503.23580*.
- Ho, J.; Jain, A.; and Abbeel, P. 2020. Denoising diffusion probabilistic models. *NeurIPS*, 33: 6840–6851.
- Ho, J.; and Salimans, T. 2022. Classifier-free diffusion guidance. *arXiv preprint arXiv:2207.12598*.
- Ke, J.; Wang, Q.; Wang, Y.; Milanfar, P.; and Yang, F. 2021. Musiq: Multi-scale image quality transformer. In *ICCV*, 5148–5157.
- Li, Y.; Zhang, K.; Liang, J.; Cao, J.; Liu, C.; Gong, R.; Zhang, Y.; Tang, H.; Liu, Y.; Demandolx, D.; et al. 2023. Lsdir: A large scale dataset for image restoration. In *Proceedings of the IEEE/CVF Conference on Computer Vision and Pattern Recognition*, 1775–1787.
- Liang, J.; Cao, J.; Sun, G.; Zhang, K.; Van Gool, L.; and Timofte, R. 2021. Swinir: Image restoration using swin transformer. In *ICCV*, 1833–1844.
- Liang, J.; Zeng, H.; and Zhang, L. 2022. Details or artifacts: A locally discriminative learning approach to realistic image super-resolution. In *CVPR*, 5657–5666.
- Lim, B.; Son, S.; Kim, H.; Nah, S.; and Mu Lee, K. 2017. Enhanced deep residual networks for single image super-resolution. In *CVPRW*, 136–144.
- Lin, X.; He, J.; Chen, Z.; Lyu, Z.; Fei, B.; Dai, B.; Ouyang, W.; Qiao, Y.; and Dong, C. 2023. DiffBIR: Towards Blind Image Restoration with Generative Diffusion Prior. *arXiv preprint arXiv:2308.15070*.
- Loshchilov, I.; and Hutter, F. 2017. Decoupled weight decay regularization. *arXiv preprint arXiv:1711.05101*.
- Rombach, R.; Blattmann, A.; Lorenz, D.; Esser, P.; and Ommer, B. 2022. High-resolution image synthesis with latent diffusion models. In *CVPR*, 10684–10695.
- Sun, L.; Wu, R.; Ma, Z.; Liu, S.; Yi, Q.; and Zhang, L. 2025. Pixel-level and semantic-level adjustable super-resolution: A dual-lora approach. In *Proceedings of the Computer Vision and Pattern Recognition Conference*, 2333–2343.
- Tao, Y.; Rongyuan, W.; Peiran, R.; Xuansong, X.; and Lei, Z. 2023. Pixel-Aware Stable Diffusion for Realistic Image Super-Resolution and Personalized Stylization. In *ECCV*.
- Wang, J.; Chan, K. C.; and Loy, C. C. 2023. Exploring clip for assessing the look and feel of images. In *AAAI*, volume 37, 2555–2563.
- Wang, J.; Yue, Z.; Zhou, S.; Chan, K. C.; and Loy, C. C. 2023a. Exploiting Diffusion Prior for Real-World Image Super-Resolution. *arXiv preprint arXiv:2305.07015*.
- Wang, X.; Xie, L.; Dong, C.; and Shan, Y. 2021. Real-esrgan: Training real-world blind super-resolution with pure synthetic data. In *ICCV*, 1905–1914.
- Wang, Y.; Yang, W.; Chen, X.; Wang, Y.; Guo, L.; Chau, L.-P.; Liu, Z.; Qiao, Y.; Kot, A. C.; and Wen, B. 2024. SinSR: Diffusion-Based Image Super-Resolution in a Single Step. In *CVPR*.
- Wang, Z.; Bovik, A. C.; Sheikh, H. R.; and Simoncelli, E. P. 2004. Image quality assessment: from error visibility to structural similarity. *IEEE TIP*, 13(4): 600–612.
- Wang, Z.; Lu, C.; Wang, Y.; Bao, F.; Li, C.; Su, H.; and Zhu, J. 2023b. ProlificDreamer: High-Fidelity and Diverse Text-to-3D Generation with Variational Score Distillation. *arXiv preprint arXiv:2305.16213*.
- Wei, P.; Xie, Z.; Lu, H.; Zhan, Z.; Ye, Q.; Zuo, W.; and Lin, L. 2020. Component divide-and-conquer for real-world image super-resolution. In *ECCV*, 101–117. Springer.
- Wu, H.; Zhang, Z.; Zhang, W.; Chen, C.; Liao, L.; Li, C.; Gao, Y.; Wang, A.; Zhang, E.; Sun, W.; Yan, Q.; Min, X.; Zhai, G.; and Lin, W. 2024a. Q-Align: Teaching LMMs for Visual Scoring via Discrete Text-Defined Levels. In Salakhutdinov, R.; Kolter, Z.; Heller, K.; Weller, A.; Oliver, N.; Scarlett, J.; and Berkenkamp, F., eds., *ICML*, volume 235 of *Proceedings of Machine Learning Research*, 54015–54029. PMLR.
- Wu, R.; Sun, L.; Ma, Z.; and Zhang, L. 2024b. One-Step Effective Diffusion Network for Real-World Image Super-Resolution. *arXiv preprint arXiv:2406.08177*.

Wu, R.; Yang, T.; Sun, L.; Zhang, Z.; Li, S.; and Zhang, L. 2024c. SeeSR: Towards Semantics-Aware Real-World Image Super-Resolution. In *CVPR*.

Xie, L.; Wang, X.; Chen, X.; Li, G.; Shan, Y.; Zhou, J.; and Dong, C. 2023. Desra: detect and delete the artifacts of gan-based real-world super-resolution models. *arXiv preprint arXiv:2307.02457*.

Yang, S.; Wu, T.; Shi, S.; Lao, S.; Gong, Y.; Cao, M.; Wang, J.; and Yang, Y. 2022. Maniqa: Multi-dimension attention network for no-reference image quality assessment. In *CVPR*, 1191–1200.

Zhang, A.; Yue, Z.; Pei, R.; Ren, W.; and Cao, X. 2024. Degradation-guided one-step image super-resolution with diffusion priors. *arXiv preprint arXiv:2409.17058*.

Zhang, K.; Liang, J.; Van Gool, L.; and Timofte, R. 2021. Designing a practical degradation model for deep blind image super-resolution. In *ICCV*, 4791–4800.

Zhang, R.; Isola, P.; Efros, A. A.; Shechtman, E.; and Wang, O. 2018a. The unreasonable effectiveness of deep features as a perceptual metric. In *CVPR*, 586–595.

Zhang, Y.; Li, K.; Li, K.; Wang, L.; Zhong, B.; and Fu, Y. 2018b. Image super-resolution using very deep residual channel attention networks. In *ECCV*, 286–301.

Zhao, Q.; Guo, C.; Zhang, T.; Zhang, J.; Jia, P.; Su, T.; Jiang, W.; and Li, C. 2025. A Systematic Investigation on Deep Learning-Based Omnidirectional Image and Video Super-Resolution. *arXiv preprint arXiv:2506.06710*.

Time-Aware One Step Diffusion Network for Real-World Image Super-Resolution

Supplementary Material

In this supplementary material, we provide the following content:

- Detailed derivation about the Variational Score Distillation loss in Section 1
- Visual comparisons of TADSR across different timesteps in Section 2
- Ablation study on the blurred MSE loss in Section 3
- Comparisons with GAN-based Real-ISR methods in Section 4
- Extended visual comparisons with SD-based Real-ISR approaches in Section 5

1. Detailed Derivation

According to the original diffusion process in SD, at step t , the current state z_t satisfies:

$$z_t = \alpha_t z_0 + \beta_t \epsilon, t = 1, 2, \dots, T, \quad (11)$$

where α_t and β_t are the scale parameters in diffusion, $\epsilon \sim \mathcal{N}(\mathbf{0}, \mathbf{I}^2)$ and z_0 is HR latent in Real-ISR task. Therefore, we can express z_0 in terms of z_t and ϵ as $z_0 = \frac{z_t - \beta_t \epsilon}{\alpha_t}$. Then, we can rewrite Eq. (2) in the main paper as follows:

$$\begin{aligned} \nabla_{\theta} \mathcal{L}_{VSD}(\hat{z}, c) &= \mathbb{E}_{t, \epsilon} \left[\omega(t) (\epsilon_{\psi}(\hat{z}_t; t, c) - \epsilon_{\phi}(\hat{z}_t; t, c)) \frac{\partial \hat{z}}{\partial \theta} \right], \\ &= \mathbb{E}_{t, \epsilon} \left[\omega(t) \frac{\alpha_t}{\beta_t} \left(\frac{(\hat{z}_t - \beta_t \epsilon_{\phi}(\hat{z}_t; t, c))}{\alpha_t} - \frac{(\hat{z}_t - \beta_t \epsilon_{\psi}(\hat{z}_t; t, c))}{\alpha_t} \right) \frac{\partial \hat{z}}{\partial \theta} \right], \\ &= \mathbb{E}_{t, \epsilon} \left[\omega(t) \frac{\alpha_t}{\beta_t} (\hat{z}_{\phi}(\hat{z}_t; t, c) - \hat{z}_{\psi}(\hat{z}_t; t, c)) \frac{\partial \hat{z}}{\partial \theta} \right], \end{aligned} \quad (12)$$

where ϵ_{ψ} is the pre-trained diffusion model (teacher model), ϵ_{ϕ} represents its replica with trainable LoRA (LoRA model), \hat{z}_{ψ} and \hat{z}_{ϕ} represent the latent images predicted by the teacher model and the LoRA model respectively, c is a text embedding of a caption describing the input image, and ω_t is a time-varying weighting function. Therefore, we can represent the VSD loss using the residual between the latent images predicted by the teacher model and the LoRA model, which is then decoded into pixel space to analyze the timestep-dependent guidance.

2. Visual Comparisons of TADSR at Different Timesteps t_s

Fig. 6 presents TADSR’s results at different timesteps t_s , demonstrating a gradual transition from fidelity to realism reconstruction as the t_s increases. Specifically: (1) In the first row, TADSR progressively generates richer eyelash textures and sharper contours; (2) The second row shows how patterned shadows gradually transform into stain-like artifacts; (3) For the third row, TADSR reconstructs plausible architectural stripes not present in the low-quality input; and (4) The fourth row reveals emerging yellow pistils in flower centers. These progressive changes evidence TADSR’s enhanced utilization of the pre-trained generative priors in SD at larger t_s , effectively balancing the fidelity-realism trade-off condition on t_s .

3. Ablation Study on the Blurred MSE Loss

To avoid gradient inconsistency arising from the ill-posed problem of the Real-ISR task while fully leveraging generative prior of SD, we introduce a blurred MSE loss to replace the original MSE loss. Specifically, we first apply a Gaussian blur to both the reconstructed image $G_{\theta}(x_L)$ and the HQ image x_H before computing the MSE loss. The blurred MSE loss can be formed as:

$$\mathcal{L}_{MSE}^{blur} = \mathcal{L}_{MSE}(G_{\theta}(x_L) * G_{t_s}, x_H * G_{t_s}). \quad (13)$$

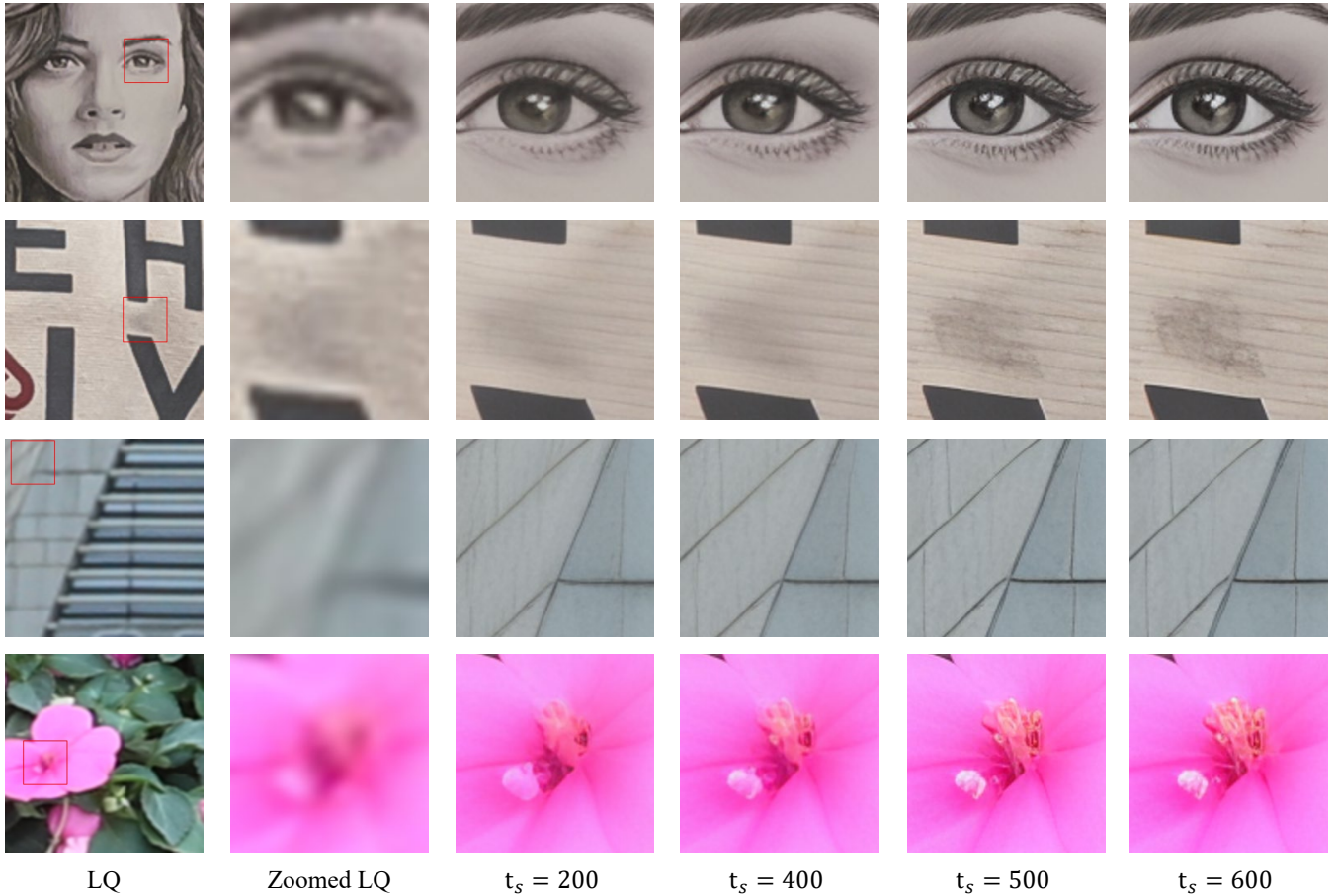


Figure 6: Vision comparisons of TADSR at different timesteps t_s . Zoom in for a better view.

Where $*$ denotes the convolution operation, G_{t_s} is the Gaussian convolution kernel whose size is determined by t_s . Let k_{t_s} as the kernel size of G_{t_s} , it satisfies:

$$k_{t_s} = 5 + 4 * \lfloor \frac{t_s}{200} \rfloor. \quad (14)$$

To validate the effectiveness of the proposed blurred MSE loss, we performed an ablation study by removing it. As shown in Tab. 4, when the blurred MSE loss is removed, the no-reference metrics degrade significantly while the reference metrics improve, demonstrating a trade-off effect where fidelity is enhanced at the expense of realism. To better align with the reference metrics, we selected TADSR’s output at $t_s = 300$. With the blurred MSE loss incorporated, TADSR achieves improvements across all metrics, indicating that this loss function enables a more optimal balance between fidelity and realism.

Table 4: Quantitative comparison of ablation study on blurred MSE loss, evaluated on DrealSR dataset

Methods	PSNR \uparrow	SSIM \uparrow	LPIPS \uparrow	MUSIQ \uparrow	MAINQA \uparrow	QALIGN \uparrow
w/o blurred MSE	29.074	0.7841	0.3056	64.732	0.6045	3.5299
TADSR ($t_s = 300$)	29.167	0.794	0.3036	65.367	0.6214	3.6069
TADSR	28.387	0.7758	0.3235	67.016	0.6309	3.7491

4. Comparisons with GAN-based Real-ISR Methods

We compare TADSR with three GAN-based Real-ISR methods: BSRGAN, RealESRGAN, and LDL. Quantitative evaluations are conducted on the DIV2K, RealSR, and DRealSR datasets, with results summarized in Tab. 5. The experimental results demonstrate that TADSR, leveraging the powerful generative priors of the pre-trained Stable Diffusion (SD) model, achieves significantly superior no-reference metrics compared to GAN-based methods.

Table 5: A comprehensive evaluation against state-of-the-art GAN-based methods across synthetic and real-world datasets. The top-performing results under each metric are marked in **red**.

Datasets	Methods	PSNR \uparrow	SSIM \uparrow	LPIPS \uparrow	CLIPQA \uparrow	MUSIQ \uparrow	MAINQA \uparrow	TOPIQ \uparrow	QALIGN \uparrow
<i>DIV2k-Val</i>	BSRGAN	24.583	0.6269	0.3351	0.5246	61.196	0.5041	0.5460	3.1708
	RealESRGAN	24.293	0.6372	0.3112	0.5277	61.058	0.5485	0.5297	3.2768
	LDL	23.828	0.6344	0.3256	0.5179	60.038	0.5328	0.5144	3.1797
	TADSR	23.815	0.6028	0.3078	0.7353	69.649	0.6443	0.7044	4.0783
<i>DrealSR</i>	BSRGAN	28.701	0.8028	0.2858	0.5092	57.165	0.4845	0.5060	2.9580
	RealESRGAN	28.615	0.8051	0.2819	0.4525	54.268	0.4903	0.4623	2.8645
	LDL	28.197	0.8124	0.2792	0.4475	53.949	0.4894	0.4518	2.8564
	TADSR	28.387	0.7758	0.3235	0.7398	67.016	0.6309	0.6758	3.7491
<i>RealSR</i>	BSRGAN	26.379	0.7651	0.2656	0.5116	63.287	0.5420	0.5505	3.1843
	RealESRGAN	25.686	0.7614	0.2710	0.4494	60.370	0.5505	0.5148	3.1073
	LDL	25.281	0.7565	0.2750	0.4555	60.928	0.5495	0.5125	3.0888
	TADSR	25.166	0.7150	0.3168	0.7283	71.182	0.6715	0.7082	3.9477

Additionally, Fig. 7 presents a visual comparison between TADSR and other GAN-based methods. The results show that TADSR reconstructs more photorealistic and natural outcomes, including higher fidelity in text and architectural structures (from the first to the third group), and more realistic rope textures (in the fourth group).

5. More Visual Comparisons with SD-based Real-ISR Methods

We provide more visual comparisons between TADSR and other SD-based SR methods in Fig. 8 and Fig. 9. Compared to other methods, TADSR consistently produces clearer, more realistic, and more natural results.

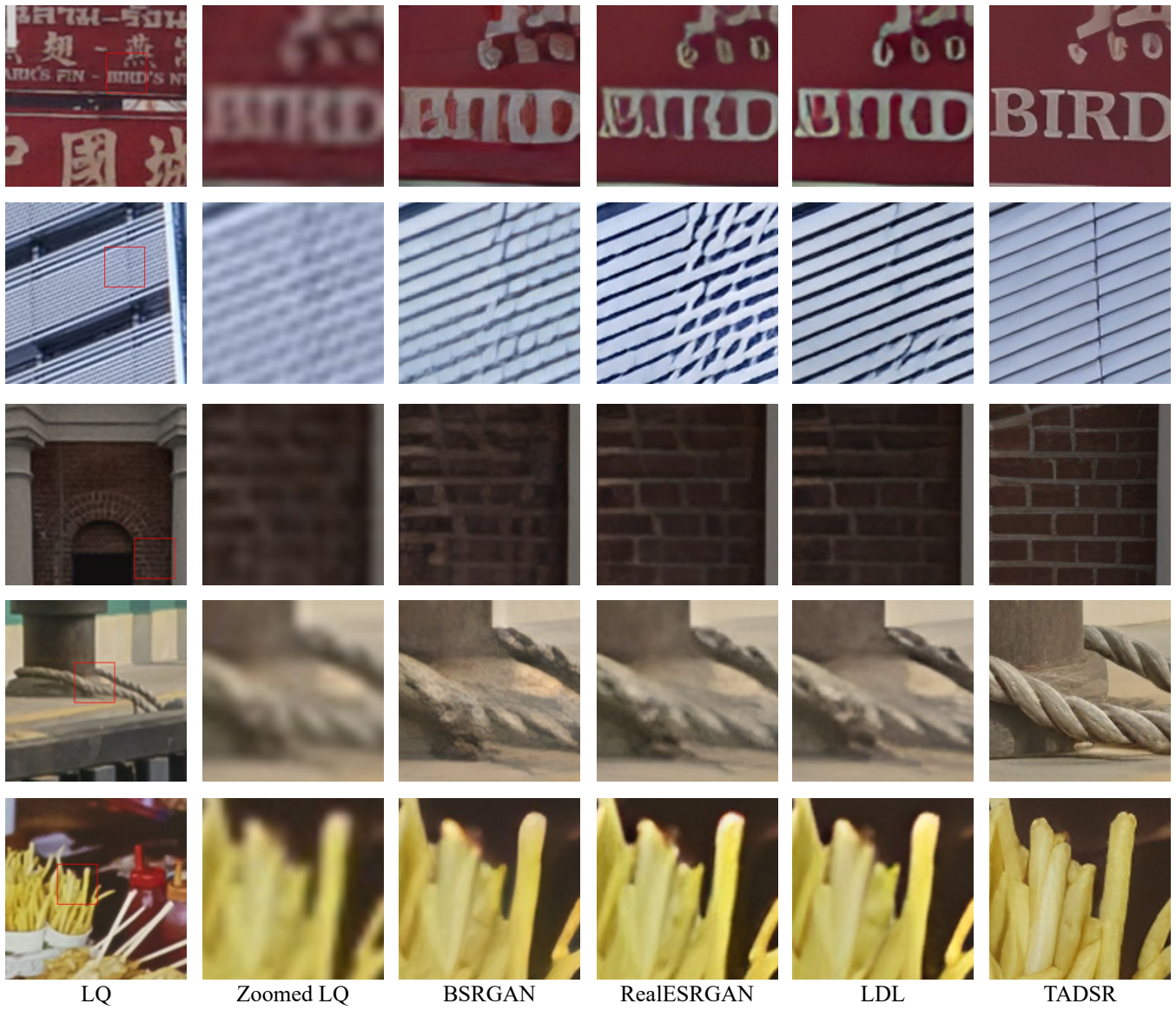


Figure 7: Vision comparisons between TADSR and GAN-based Real-ISR methods. Zoom in for a better view.

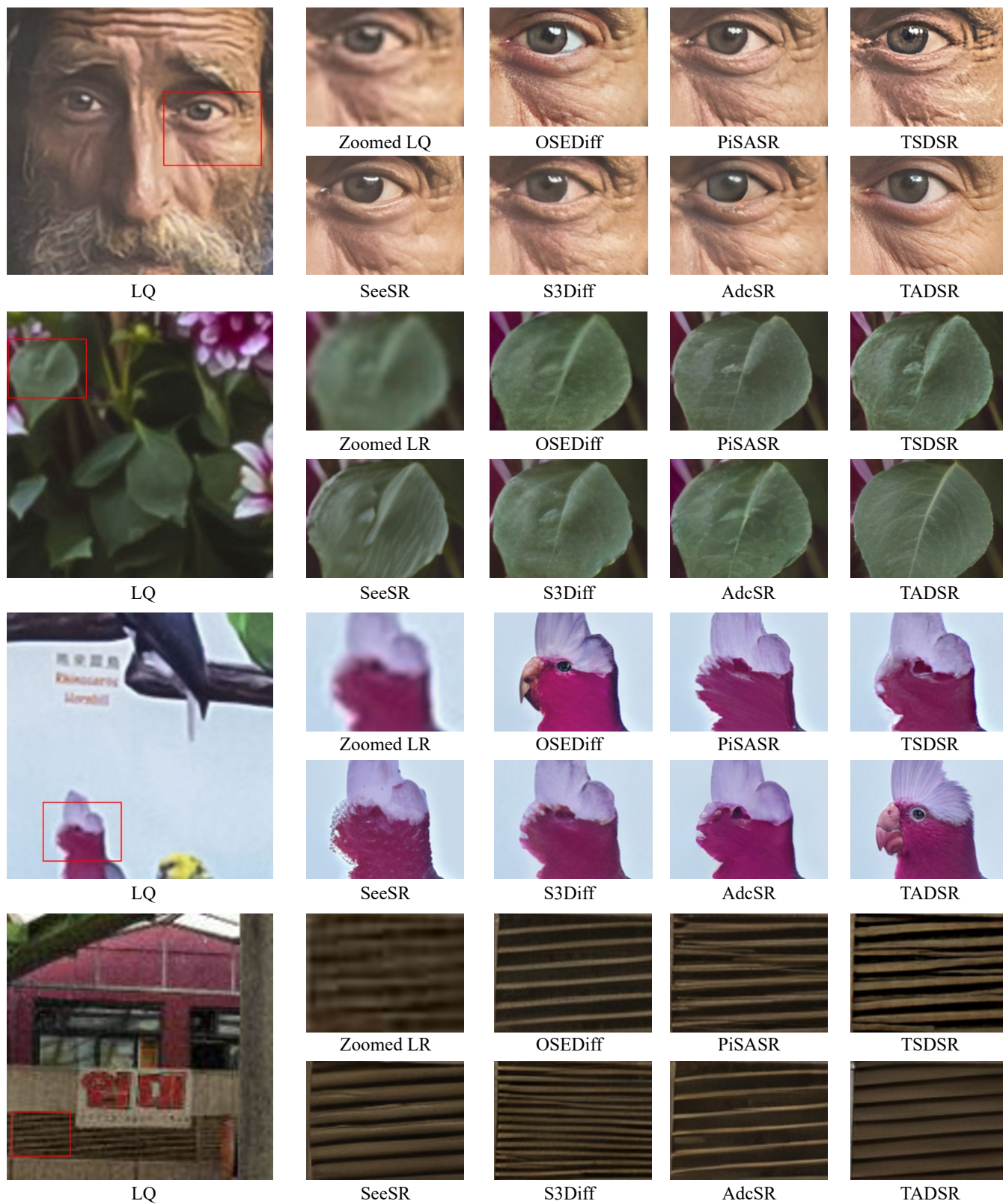


Figure 8: Vision comparisons between TADSR and SD-based Real-ISR methods. Zoom in for a better view.

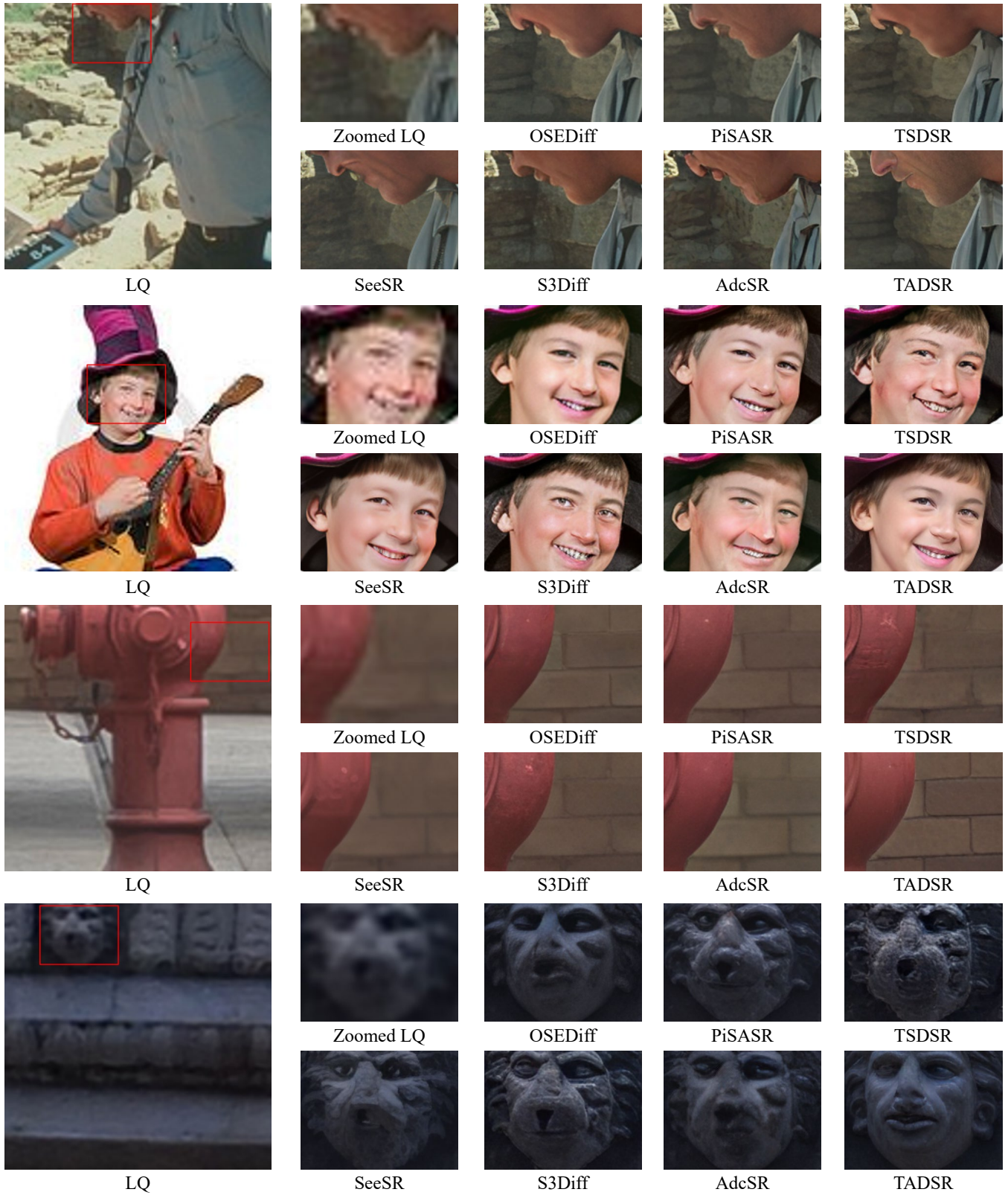


Figure 9: Vision comparisons between TADSR and SD-based Real-ISR methods. Zoom in for a better view.